





Effect of tensile and compressive strain on the gate leakage current and inverse piezoelectric effect in AlGa_N/Ga_N HEMT devices

Cite as: Appl. Phys. Lett. **125**, 032101 (2024); doi: [10.1063/5.0197849](https://doi.org/10.1063/5.0197849)

Submitted: 15 January 2024 · Accepted: 1 July 2024 ·

Published Online: 15 July 2024



Yiqun Zhang,  Hui Zhu, ^{a)}  Xing Liu, Zhirang Zhang, Chao Xu, Keyu Ren,  Chunsheng Guo, Yamin Zhang,  Lixing Zhou,  and Shiwei Feng 

AFFILIATIONS

School of Microelectronics, Faculty of Information Technology, Beijing University of Technology, Beijing 100124, China

^{a)} Author to whom correspondence should be addressed: zhuhui@bjut.edu.cn

ABSTRACT

The influence of external strain on the gate leakage current of AlGa_N/Ga_N high-electron-mobility transistors was studied. The magnitude of the leakage current increased by 39% under 0.1% tensile strain but decreased by 23% under −0.1% compressive strain. The leakage current obeyed the Poole–Frenkel conduction mechanism, demonstrating a decrease/increase in the barrier height for electron emission from the trap state into the continuum dislocation state. Furthermore, the magnitude of critical reverse stressing voltage for the onset of degradation induced by the inverse piezoelectric effect became lower/higher under tensile/compressive strain compared with that of the initial state, which was attributed to the modification of the total stress in the film. In addition, using the transient current method, it was established that the detrapping time constant for the traps in the AlGa_N barrier increased as a result of the tensile strain, which is ascribed to movement of the dislocation level away from the conduction band.

Published under an exclusive license by AIP Publishing. <https://doi.org/10.1063/5.0197849>

The beneficial properties of gallium nitride (Ga_N) materials enable the application of AlGa_N/Ga_N high-electron-mobility transistors (HEMTs) in high-power and high-frequency electronics.^{1–4} The AlGa_N/Ga_N HEMT offers several advantages, such as high thermal stability, high breakdown field strength, and high electron-saturation velocity.^{5–7} Owing to the piezoelectric property of Ga_N-based materials,^{8–10} their electrical characteristics can be modulated by applying external stress/strain.^{11–14} It is possible to adjust the bandgap and change the conduction of the two-dimensional electron gas (2DEG) channel by tailoring the stress effect on the AlGa_N/Ga_N heterostructure.¹⁴ However, there is a lack of studies concerning changes in the gate leakage current under external strain, which is an important reliability issue related to the AlGa_N barrier. Furthermore, because of variations in the strain state in the film under external stress, the correlated **inverse piezoelectric effect (IPE)** must also be considered. The IPE results from the extra tensile stress in the AlGa_N barrier under the application of a high electric field between the gate and drain,¹⁵ causing the formation of defects and an increase in gate leakage current, which severely limits the performance of HEMT devices in high-power applications.^{15–18} Upon straining, mechanical deformation alters the intrinsic lattice mismatch strain, which is expected to

affect the IPE-induced degradation.¹⁹ In addition, the defects and traps in the AlGa_N barrier are closely related to the gate leakage and IPE degradation. An analysis of the change in trapping phenomenon and trap levels in the AlGa_N barrier under external strain is also necessary for a systematic study of the strain effect and optimization of the device performance.

In this study, we examined the gate leakage current in AlGa_N/Ga_N HEMTs and the IPE under tensile and compressive strains. The variation in gate leakage was analyzed by determining the fitting of the conduction mechanism. The change in critical voltage stress for the electrical degradation due to IPE was investigated under different strains and compared with the theoretical derivation. The changes in trap time constant and activation energy in the AlGa_N barrier were also studied to investigate the physical mechanism of the strain effect on the AlGa_N/Ga_N HEMT.

Herein, the AlGa_N/Ga_N HEMT structures were grown on 80 μm-thick sapphire substrates as shown in Fig. 1. First, a 100 nm-thick AlN nucleation layer was grown on a sapphire substrate. Next, 2.5 μm-thick undoped Ga_N buffer and 20 nm-thick undoped Al_{0.21}Ga_{0.79}N barrier layers were sequentially deposited by metal-organic chemical vapor deposition. The device was passivated with

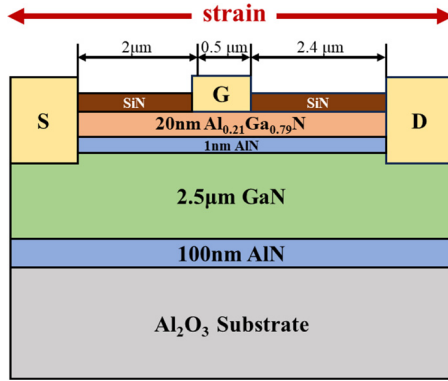


FIG. 1. A schematic diagram of the AlGaIn/GaN HEMT device structure. The red arrows indicate the direction of strain.

100 nm Si_3N_4 to prevent surface oxidation and degradation. The source–drain contacts were composed of Ti/Al/Pt/Au Ohmic contacts, and the gate contacts were composed of Ni/Au Schottky contacts.

External strain was applied along the device channel length direction using a four-point bending test rig, which was described in detail in our previous work.^{14,20} Under the external strain, the electrical characteristics of the device were measured using an Agilent B1500A parameter analyzer. The bending experiment was repeated for three devices to ensure the results' reliability. The reverse voltage step stress, denoted as V_{Gstress} , was applied to the gate from -10 to -60 V in steps of -10 V,¹⁶ while the external strain was exerted on the device. Each voltage stress cycle lasted for 100 s and was then removed, and the measurements of the electrical characteristics were performed during this interval.

Figure 2(a) shows the change in gate leakage current curve ($I_{\text{G}}-V_{\text{G}}$) under the application of different strains. The magnitude of I_{G} increased under tensile strain but decreased under compressive strain. The inset of Fig. 2(a) shows the variation in $|I_{\text{G}}|$ ($V_{\text{G}} = -3$ V) as a function of strain. At a tensile strain of 0.1%, taking average values for three devices, the magnitude of I_{G} increased by 39%, and at a compressive strain of -0.1% , the $|I_{\text{G}}|$ decreased by 23%. After the maximum strain was applied, the strain was gradually reduced to return the sample to its flat state. The $I_{\text{G}}-V_{\text{G}}$ curve shifted back toward its strain-free state (not shown here), and the inset confirms the recovery of the current value.

The reverse gate leakage mechanism is consistent with Poole–Frenkel (PF) emission based on the fitting of current density (J) vs electric field (E). The details of the conduction mechanism analysis have been published elsewhere.¹⁶ Figure 2(b) shows the $\ln(J_{\text{PF}}/E)$ vs $E^{1/2}$ characteristics for the gate voltage ranging from -4 to -2.58 V, revealing a linear relationship, as predicted by the following equation for PF emission:^{21,22}

$$\ln\left(\frac{J_{\text{PF}}}{E}\right) = \frac{q}{kT} \sqrt{\frac{q}{\pi\epsilon_i}} \sqrt{E} + b(T), \quad (1)$$

where q is the electron charge, ϵ_i is the dielectric constant of AlGaIn at high frequency, k is the Boltzmann constant, and T is the absolute temperature. The y-intercept of the plot is represented by $b(T)$, which is expressed in the following equation:

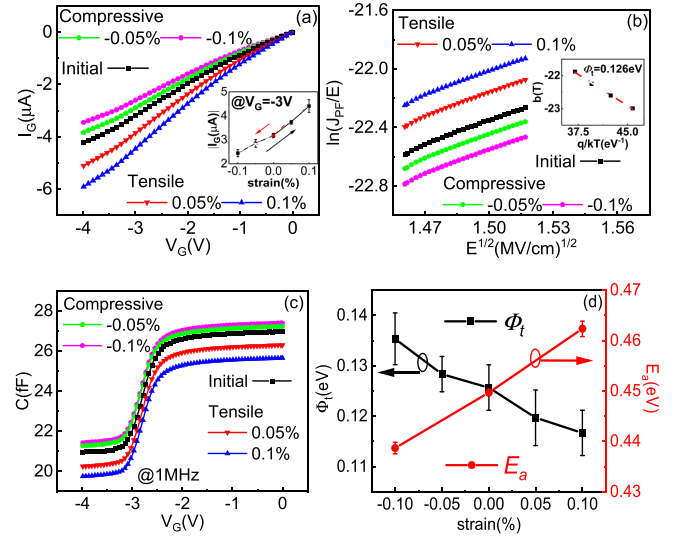


FIG. 2. (a) Gate leakage current vs voltage characteristics for the AlGaIn/GaN HEMT measured under the application of different strains. The inset shows the change in I_{G} ($V_{\text{G}} = -3$ V) with respect to strains. The arrows indicate the change as the strain increases and decreases. (b) The $\ln(J_{\text{PF}}/E)$ vs $E^{1/2}$ plot at different strains. The inset shows the plot of $b(T)$ vs q/kT for the initial device. (c) Capacitance vs voltage curves for the HEMT under different strains. (d) The barrier height Φ_t for electron emission from the trap state into the continuum dislocation state, and the activation energy E_a of the dislocation-trap state under different strains.

$$b(T) = -\frac{q\Phi_t}{kT} + \ln(B), \quad (2)$$

where B is a constant, and Φ_t is the barrier height for electron emission from the trap state to the continuum of electronic states associated with the conductive dislocation.²³ The electric field E across the AlGaIn barrier can be calculated as follows:

$$E = \frac{q(P - n_s)}{\epsilon}, \quad (3)$$

where ϵ is the dielectric constant of the AlGaIn barrier, and n_s is the concentration of the 2DEG, which can be determined by integrating over the capacitance–voltage curve,²⁴ as shown in Fig. 2(c). P is the polarization-induced sheet charge density at the heterogeneous interface,

$$P = P_{\text{PE}}(\text{AlGaIn}) + P_{\text{SP}}(\text{AlGaIn}) - P_{\text{SP}}(\text{GaN}) - P_{\text{PE}}(\text{GaN}). \quad (4)$$

The spontaneous polarizations in AlGaIn and GaN were obtained from previous reports:²⁵ $P_{\text{SP}}(\text{Al}_{0.29}\text{Ga}_{0.71}\text{N}) = -0.040 \text{ C m}^{-2}$ and $P_{\text{SP}}(\text{GaN}) = -0.029 \text{ C m}^{-2}$. The piezoelectric polarization in the AlGaIn barrier is $P_{\text{PE}}(\text{Al}_{0.29}\text{Ga}_{0.71}\text{N}) = -0.009 \text{ C m}^{-2}$, whereas the $P_{\text{PE}}(\text{GaN})$ is originally zero because the GaN layer is relaxed in the initial device.¹⁴ As a result, the net polarization sheet charge density P without external strain was calculated to be 0.020 C m^{-2} . From the $\ln(J_{\text{PF}}/E)$ vs $E^{1/2}$ plots under different temperatures (not shown here), the change in $b(T)$ was extracted and plotted as a function of q/kT , as shown in the inset of Fig. 2(b). The trap emission barrier height Φ_t in the initial state was fitted from the linear slope, revealing a value of $\sim 0.126 \text{ eV}$, which is consistent with the previously reported value.^{16,21}

TABLE I. Parameters used in the calculation of polarization charge density P and total tensile stress σ_{total} in the $\text{Al}_{0.21}\text{Ga}_{0.79}\text{N}$ barrier layer.¹⁷

Parameters	GaN	AlN	$\text{Al}_{0.21}\text{Ga}_{0.79}\text{N}$
e_{31} (C/m ²)	-0.49	-0.6	-0.513
e_{33} (C/m ²)	0.73	1.46	0.883
C_{11} (GPa)	350	356	351.26
C_{12} (GPa)	110	121	112.31
C_{13} (GPa)	104	113	105.89
C_{33} (GPa)	405	373	398.28

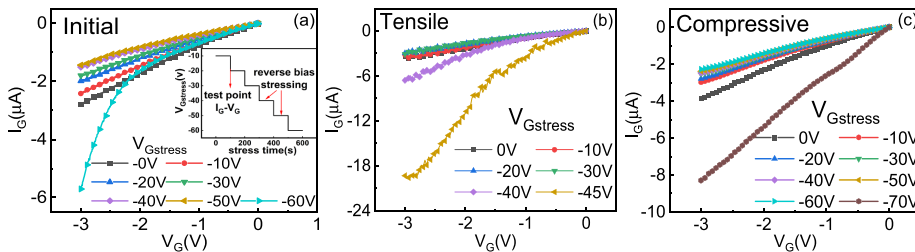
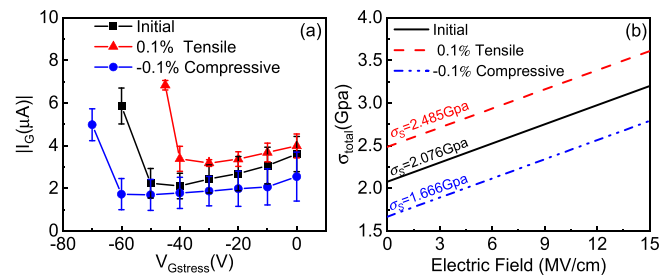
When an external strain s is applied, the polarization charge density changes because of the piezoelectric effect, which can be expressed by

$$P_{\text{PE}}(\text{GaN}) = e_{31}(\text{GaN})s, \quad (5)$$

where e_{ij} is the piezoelectric tensor, which is given in Table I. According to the strain-modified P and n_s , the electric field was calculated using Eq. (3) for different strains. From Fig. 2(b), the $\ln(J_{\text{PF}}/E)$ vs $E^{1/2}$ curve still exhibits a linear relationship, indicating that the reverse gate leakage current under strain still obeys PF conduction. However, the intercepts of $\ln(J_{\text{PF}}/E)$ vs $E^{1/2}$ changed, and the corresponding emission barrier height Φ_t was found to decrease with tensile strain but increase with compressive strain. According to the PF emission mechanism, the reduction of Φ_t under tensile strain implies that the electron emission from the trap state into the continuum dislocation state becomes easier, resulting in increased reverse gate leakage current. Conversely, the rise in Φ_t under compressive strain is consistent with the decrease in $|I_G|$.

The reverse bias stressing experiments as shown in the inset of Fig. 3(a) were conducted to assess the effect of strain on the IPE. The changes in gate leakage current I_G that occurred after the application of different voltage stresses V_{Gstress} under no strain, 0.1% tensile strain, and -0.1% compressive strain are shown in Figs. 3(a)–3(c). The change in I_G is divided into two stages. First, the magnitude of I_G decreased with a decrease in V_{Gstress} , suggesting that some inherent traps were filled by gate-injected electrons at this stage.^{15,26} Then, a sudden rise in the magnitude of I_G was observed when a critical voltage of V_{Gstress} was reached, which indicates the typical irreversible degradation caused by the IPE, as reported in previous studies.^{16,17,27,28}

Figure 4(a) shows the shift in gate leakage current ($V_G = -3$ V, $V_D = 0$ V) with respect to the voltage stress. The critical V_{Gstress} required for IPE-induced degradation was -60 V under no strain but increased to -45 V under 0.1% tensile strain and decreased to -70 V under -0.1% compressive strain.

**FIG. 3.** Gate current vs voltage characteristics measured after applying different values of the voltage step stress V_{Gstress} for HEMTs under (a) zero strain, (b) 0.1% tensile strain, and (c) -0.1% compressive strain. The inset shows the voltage sequence diagram.**FIG. 4.** (a) Comparison of the change in gate current ($V_G = -3$ V) after each voltage stress application under different strains. (b) Total tensile stress with the application of an electric field for the HEMT under different external strains.

For the AlGaIn/GaN heteroepitaxy growth structure, there is a built-in lattice mismatch between the AlGaIn barrier layer and the GaN buffer layer. This results in substantial in-plane tensile stress and stored elastic energy in the AlGaIn barrier.¹⁵ Owing to the IPE, the application of a high voltage induces an electric field that increases the tensile stress in the AlGaIn barrier. Joh *et al.* derived an equation to calculate the total tensile stress in the AlGaIn barrier,¹⁵

$$\sigma_{\text{total}} = \left(C_{11} + C_{12} - 2 \times \frac{C_{13}^2}{C_{33}} \right) \times s + \left(\frac{C_{13} \times e_{33}}{C_{33}} - e_{31} \right) \times E \quad (6)$$

$$\equiv \sigma_s + \sigma_E,$$

where C_{ij} is the elastic stiffness constant, σ_s denotes the in-plane tensile stress corresponding to mechanical strain, and σ_E represents the stress induced by the electric field due to the IPE. For the initial device, the strain is caused by lattice mismatch between AlGaIn and GaN, which can be calculated according to $s = (a_{\text{GaN}} - a_{\text{AlGaIn}})/a_{\text{AlGaIn}}$. The lattice constant of this epitaxial GaN layer is $a_{\text{GaN}} = 0.319$ nm, according to our x-ray diffraction result.¹⁴ The lattice constant of relaxed AlGaIn is $a_{\text{AlGaIn}} = 0.317$ nm.²⁵ Based on the parameters listed in Table I, the total stress in the AlGaIn barrier can be calculated according to Eq. (6) and the theoretical result is plotted in Fig. 4(b). A linear dependence on the applied electric field is observed. The y-intercept corresponds to the as-grown in-plane tensile stress σ_s , equivalent to 2.076 GPa, which is lower than the value reported in [17]. This is attributed to the lower degree of lattice mismatch in the $\text{Al}_{0.21}\text{Ga}_{0.79}\text{N}$ structure used herein. When a critical electric field (voltage) stress is applied, σ_{total} is increased beyond this stress by the IPE. The stress relaxes through the formation of defects, and the reverse bias gate current increases suddenly.

When an external strain is applied, the lattice constant of GaN is increased by tensile strain and reduced by compressive strain. Consequently, the lattice mismatch strain and the corresponding

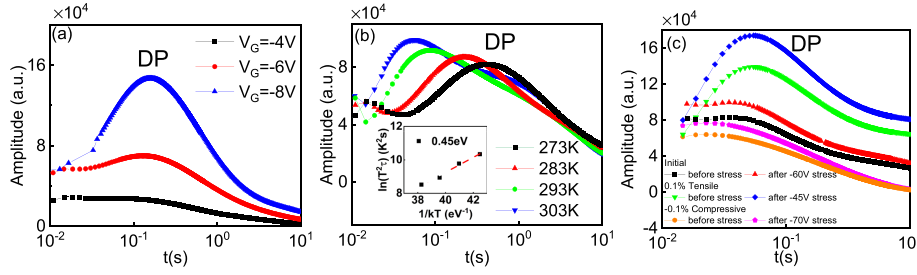


FIG. 5. (a) Time-constant spectra for detrapping after application of the trapping pulses with $V_D = 0$ V and various V_G from -4 to -8 V. (b) Time-constant spectra at various temperatures. The inset shows the Arrhenius plot of DP. (c) Comparison of time-constant spectra between the initial state and the state after application of the critical voltage stress at different strains.

in-plane stress increased under the external tensile strain but decreased under the compressive strain. In contrast, the σ_E due to the electric field is not affected. Therefore, the σ_{total} vs E curve exhibits an upward or downward translation along the y-axis, as shown in Fig. 4(b). Under tensile strain, σ_s (2.485 GPa) as estimated from the 0.1% elongation in GaN lattice constant becomes higher than that in the initial device, and then a lower critical electric field is required to achieve the onset of the IPE-induced degradation for a fixed critical σ_{total} . Under compressive strain, σ_s (1.666 GPa) is lower than that in the initial device, and a higher critical electric field is required to initiate IPE-induced degradation. The theoretical derivation of the external strain effect is consistent with our experimental results.

Both the gate leakage current and the IPE are closely related to the defects and traps in the AlGaIn barrier. Transient current measurements were used to identify the change in trap states under external strain. During the measurements, the drain and gate voltages were simultaneously pulsed to induce carrier trapping. Immediately after removing the 5 s trapping pulse, we monitored the transient recovery over a length of time with the monitoring voltages fixed at $V_{GS} = 1$ V and $V_{DS} = 0.5$ V. A detrapping behavior, denoted as DP, was identified on the time-constant spectrum after the off-state filling pulse ($V_G = -4$ V, $V_D = 0$ V), as shown in Fig. 5(a). Analysis of the detrapping peak has been published elsewhere.^{14,16,29} The peak appeared when the channel was pinched off and increased in amplitude with decrease in the trapping voltage, as shown in Fig. 5(a). This behavior may originate from traps located below the gate, which capture electrons from the gate injection current. Figure 5(b) shows the DP's time-constant spectra at various temperatures, which shift negatively with increasing temperature. Based on the Arrhenius plot shown in the inset of Fig. 5(b), the activation energy was determined to be 0.450 eV. Traps in the AlGaIn barrier under the gate with energy levels of nearly 0.450 eV have been reported previously.³⁰

After the application of 0.1% tensile strain, the DP's time-constant spectra showed a rightward shift, as shown in Fig. 5(c). The measured time constant τ corresponds to the time when the maximum number of charge carriers is released from the trap sites. We derived the difference in DP's activation energy E_a according to the difference in time constants between the strained $\tau(s)$ and the initial value $\tau(0)$,¹⁴

$$\Delta E_a = E_a(s) - E_a(0) = kT \ln \frac{\tau(s)}{\tau(0)}, \quad (7)$$

where $E_a(s)$ and $E_a(0)$ represent the activation energy of DP under strain and initial state, respectively. For the device under 0.1% tensile strain, the activation energy increased to 0.461 eV, and for the device under -0.1% compressive strain, the activation energy reduced to 0.439 eV, as shown in Fig. 2(d). Furthermore, for the device under

different strain states, we performed the reverse bias stressing. From Fig. 5(c), all the detrapping peak amplitudes increased after the critical voltage stress was applied. This confirms the degradation mechanism, showing that the trap densities in the AlGaIn barrier increased as a result of the IPE.¹⁶

According to the simulation result,³¹ the conduction band of AlGaIn tilts downward/upward with increase in the tensile/compressive strain. However, the theoretical variation ($\sim 5 \times 10^{-4}$ eV at -0.1% compressive strain)³¹ is much smaller than the measured ΔE_a , indicating that the energy level of DP should move because of the application of external strain. Therefore, changes in the energy band diagram and trap level under tensile and compressive strain are illustrated in Figs. 6(a) and 6(b). The gate leakage current flow is dominated by the PF emission of electrons from the trap states to the continuum dislocation-related trap states. The emission barrier height is Φ_t , which decreased/increased as a result of the tensile/compressive strain. Moreover, the activation energy E_a of DP in the AlGaIn barrier, as determined using the transient current method, displays an opposite changing trend (but a similar variation magnitude) with Φ_t , as shown in Fig. 2(d). Therefore, it is reasonable to conclude that the DP originates from the continuum dislocation traps in the AlGaIn barrier. This dislocation level is 0.126 eV above the trap state and 0.450 eV below the conduction band edge of AlGaIn. According to the Schottky barrier height of 0.68 eV,³² the trap level lies 0.1 eV above the metal Fermi level. When the device is subjected to tensile strain, the dislocation level moves away from the conduction band, inducing a reduction in Φ_t but an increase in E_a .

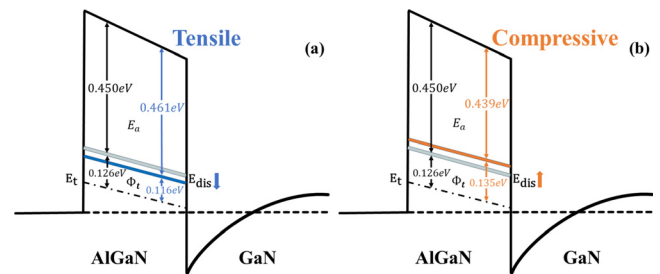


FIG. 6. Schematic of the change in energy band diagram under (a) tensile and (b) compressive strains, showing the trap and dislocation states for the AlGaIn barrier based on the measured trap emission barrier height Φ_t and activation energy E_a . The dashed-dotted line represents the trap level. The gray band represents the dislocation level in the initial state. The blue and orange bands represent the dislocation levels under tensile and compressive strains, respectively. The arrows indicate the movement direction of the dislocation level due to external strains.

In summary, the change in gate leakage current and IPE due to the external strain was investigated. **The leakage current value increased with increase in the tensile strain but decreased with increase in the compressive strain.** The variation in emission barrier height of electrons from the trap state to the continuum dislocation-trap state was determined from the fitting of the PF conduction mechanism under different strains. Furthermore, IPE-induced degradation was enhanced by tensile strain but mitigated by compressive strain. This is attributed to the rise/reduction in the total tensile stress in the AlGa_N barrier under external tensile/compressive strains. Analysis of the transient current characteristics revealed that the time constant of the detrapping behavior increased/decreased as a result of the tensile/compressive strain. Considering the relationship between the time constant and the activation energy of the trapped carriers, we found that the energy level of dislocation traps in the AlGa_N barrier moved away from the conduction band under tensile strain and moved closer to the conduction band under compressive strain. These results help clarify the gate leakage mechanisms and IPE correlated with the high reverse bias in AlGa_N/Ga_N devices, which is crucial for evaluating their reliability, strain-modulated electrical properties, and high-voltage performance.

This work was supported in part by the National Key R&D Program of China under Grant No. 2023YFB4604400, in part by the National Natural Science Foundation of China under Grant Nos. 62374012 and 62334002, and in part by the Beijing Municipal Commission of Education under Grant No. KM202010005033.

AUTHOR DECLARATIONS

Conflict of Interest

The authors have no conflicts to disclose.

Author Contributions

Yiqun Zhang: Investigation (equal); Methodology (equal); Writing – original draft (equal). **Hui Zhu:** Supervision (equal); Validation (equal); Writing – review & editing (equal). **Xing Liu:** Methodology (equal). **Zhirang Zhang:** Methodology (equal). **Chao Xu:** Methodology (equal). **Keyu Ren:** Methodology (equal). **Chunsheng Guo:** Resources (equal). **Yamin Zhang:** Resources (equal). **Lixing Zhou:** Resources (equal). **Shiwei Feng:** Methodology (equal).

DATA AVAILABILITY

The data that support the findings of this study are available within the article.

REFERENCES

- ¹K. Q. Zhu, W. Feng, Y. F. Zhu, Q. F. Ding, Y. K. Wang, Y. Xiao, L. Jin, H. Qin, and H. J. Sun, *Appl. Phys. Lett.* **121**, 081101 (2022).
- ²L. Nela, M. Xiao, Y. Zhang, and E. Matioli, *Appl. Phys. Lett.* **120**, 190501 (2022).
- ³H. Ye, M. Gaevski, G. Simin, A. Khan, and P. Fay, *Appl. Phys. Lett.* **120**, 103505 (2022).
- ⁴Y. Zhang, Y. Dong, K. Chen, K. Dang, Y. Yao, B. Wang, J. Ma, W. Liu, X. Wang, J. Zhang, and Y. Hao, *Appl. Phys. Lett.* **122**, 142105 (2023).
- ⁵H. Nakai, M. Sugiyama, and S. F. Chichibu, *Appl. Phys. Lett.* **110**, 181102 (2017).
- ⁶T. H. Chang, K. L. Xiong, S. H. Park, G. Y. Z. Q. Ma, and J. Han, *Sci. Rep.* **7**, 6360 (2017).
- ⁷L. Lari, T. Walther, M. H. Gass, L. Geelhaar, C. Chèze, H. Riechert, T. J. Bullough, and P. R. Chalker, *J. Cryst. Growth* **327**, 27 (2011).
- ⁸H. Zhang, E. J. Miller, E. T. Yu, C. Poblentz, and J. S. Speck, *Appl. Phys. Lett.* **84**, 4644 (2004).
- ⁹B. Liu, Y. W. Lu, G. R. Jin, Y. Zhao, X. L. Wang, Q. S. Zhu, and Z. G. Wang, *Appl. Phys. Lett.* **97**, 262111 (2010).
- ¹⁰B. S. Kang, S. Kim, F. Ren, J. W. Johnson, R. J. Therrien, P. Rajagopal, J. C. Roberts, E. L. Piner, K. J. Linthicum, S. N. G. Chu, K. Baik, B. P. Gila, C. R. Abernathy, and S. J. Pearton, *Appl. Phys. Lett.* **85**, 2962 (2004).
- ¹¹W. Wang, J. Chen, J. S. Lundh, S. Shervin, S. K. Oh, S. Pouladi, Z. Rao, J. Y. Kim, M.-K. Kwon, X. Li, S. Choi, and J.-H. Ryou, *Appl. Phys. Lett.* **116**, 123501 (2020).
- ¹²B. S. Kang, S. Kim, J. Kim, F. Ren, K. Baik, S. J. Pearton, B. P. Gila, C. R. Abernathy, C.-C. Pan, G.-T. Chen, J.-I. Chyi, V. Chandrasekaran, M. Sheplak, T. Nishida, and S. N. G. Chu, *Appl. Phys. Lett.* **83**, 4845 (2003).
- ¹³C. M. Jeon and J.-L. Lee, *Appl. Phys. Lett.* **86**, 172101 (2005).
- ¹⁴C. Wang, H. Zhu, S. Wang, D. P. Chu, K. Liu, L. Jin, R. Li, J. Liu, S. W. Feng, C. S. Guo, and Y. M. Zhang, *IEEE Trans. Electron Devices* **67**, 449 (2020).
- ¹⁵J. Joh, F. Gao, T. Palacios, and J. A. del Alamo, *Microelectron. Reliab.* **50**, 767 (2010).
- ¹⁶Z. W. Yao, H. Zhu, Y. L. Li, N. Xie, Y. R. Sun, Y. Q. Zhang, X. Liu, and Z. R. Zhang, *Semicond. Sci. Technol.* **38**, 055008 (2023).
- ¹⁷Q. Zhu, X. H. Ma, B. Hou, M. Wu, J. J. Zhu, L. Yang, M. Zhang, and Y. Hao, *IEEE Access* **8**, 35520 (2020).
- ¹⁸C. De Santi, M. Meneghini, G. Meneghesso, and E. Zanoni, *IET Power Electron.* **11**, 668 (2018).
- ¹⁹S. Mishra, K. Guda Vishnu, and A. Strachan, *J. Appl. Phys.* **129**, 075701 (2021).
- ²⁰N. Xie, H. Zhu, Y. Q. Zhang, Z. Huang, Z. X. Fang, Z. Liu, D. Li, S. W. Feng, C. S. Guo, Y. M. Zhang, B. Liu, L. X. Zhou, X. Liu, Y. R. Sun, Z. R. Zhang, Y. L. Li, and Z. W. Yao, *IEEE Trans. Electron Devices* **70**, 544 (2023).
- ²¹D. Yan, H. Lu, D. Cao, D. Chen, R. Zhang, and Y. Zheng, *Appl. Phys. Lett.* **97**, 153503 (2010).
- ²²S. Turuvekere, N. Karumuri, A. A. Rahman, A. Bhattacharya, A. DasGupta, and N. DasGupta, *IEEE Trans. Electron Devices* **60**, 157 (2013).
- ²³W. Chikhaoui, J.-M. Bluet, M.-A. Poisson, N. Sarazin, C. Dua, and C. Bru-Chevallier, *Appl. Phys. Lett.* **96**, 072107 (2010).
- ²⁴J. Zhao, Z. Lin, T. D. Corrigan, Z. Wang, Z. You, and Z. Wang, *Appl. Phys. Lett.* **91**, 173507 (2007).
- ²⁵O. Ambacher, B. Foutz, J. Smart, J. R. Shealy, N. G. Weimann, K. Chu, M. Murphy, A. J. Sierakowski, W. J. Schaff, and L. F. Eastman, *J. Appl. Phys.* **87**, 334 (2000).
- ²⁶L. Shi, S. W. Feng, Y. M. Zhang, B. B. Shi, and K. Liu, *IEEE Electron Device Lett.* **36**, 321 (2015).
- ²⁷H. Shiomi, A. Ueda, T. Tohei, Y. Imai, T. Hamachi, K. Sumitani, S. Kimura, Y. Ando, T. Hashizume, and A. Sakai, *Appl. Phys. Express* **14**, 095502 (2021).
- ²⁸K. R. Bagnall and E. N. Wang, *Rev. Sci. Instrum.* **87**, 061501 (2016).
- ²⁹X. Zheng, S. Feng, Y. Zhang, X. He, and Y. Wang, *IEEE Trans. Electron Devices* **64**, 1498 (2017).
- ³⁰J. Joh and J. A. del Alamo, *IEEE Trans. Electron Devices* **58**, 132 (2011).
- ³¹X. Wang, R. Yu, C. Jiang, W. Hu, W. Wu, Y. Ding, W. Peng, S. Li, and Z. L. Wang, *Adv. Mater.* **28**, 7234 (2016).
- ³²S. Chakraborty and T. W. Kim, *Micromachines* **13**, 84 (2022).